Electronic Supplementary Material (ESI) for Inorganic Chemistry Frontiers.

This journal is © the Partner Organisations 2022

Electronic Supplementary Information for

Understanding the ultraviolet, green, red, near infrared and infrared emission properties of bismuth halide double perovskite

Anjun Huang,[a] Mingzhe Liu,[b] Chang-Kui Duan,[b] Ka-Leung Wong,[*a] and Peter A. Tanner[*a]

[a]Department of Chemistry, Hong Kong Baptist University, 224 Waterloo Road, Kowloon Tong, Hong Kong, China. E-mail: klwong@hkbu.edu.hk; peter.a.tanner@gmail.com

[b]CAS Key Laboratory of Microscale Magnetic Resonance, University of Science and Technology of China, Hefei 230026, China.

Table of Contents

S1. Computation method

S1a. Parameter settings. The first-principles calculations were carried out with the projector augmented wave method[1] implemented in the Vienna *ab initio* simulation package code.[2,3] The generalized gradient approximation of the Perdew-Burke-Ernzerhof (PBE) functional[4] was applied for the exchange correlation functional, and the spin-orbit coupling (SOC) interaction is included for a more accurate description of Bi.

S2. Computation results

Density functional calculations have previously been carried out to investigate the band structure in $Cs_2NaBiCl_6$.[7-10] The calculation with the PBE density functional shows that $Cs_2NaBiCl_6$ has an indirect band gap of 3.01 eV, as plotted in **Fig. S1(a)**, with the density of states shown in **Fig. S1(b)**. This is comparable with the reported value of 2.98 eV from a PBE level calculation.[9] Other reference values are 4.64 eV and 5.22 eV from PBE0 calculation with mixing parameter α = 0.25[11] and 0.32,[5] respectively. Previous experimental measurements of the optical band gap of $Cs_2NaBiCl_6$ range from 3.35 eV,[10] 3.41 eV[12] and 3.75 eV,[13] being smaller than the band gap of the isostructural halide double perovskites like $Cs_2Na\mathit{M}Cl_6$ (M = Sc^{3+}, Y^{3+}, La^{3+}) by more than 2 eV, due to the domination of the much lower $6s \rightarrow 6p$ transition of Bi^{3+}, other than the transitions between the Cl-dominated valence band (VB) to the cation ion *M*-dominated conduction band (CB).

The electric dipole transition is forbidden between the CB maximum (CBM) and VBM states at the Γ point, **Fig. S1(c)**. The absorption spectrum and joint density of states (DOS) of the VB to CB transition in **Fig. S1(d)** show the absorption edge and peaks. The PBE0 (α = 0.32) calculation gives the $6s^2 \rightarrow 6s6p$ ($^1S_0 \rightarrow {}^3P_{0,1}$) transition of Bi^{3+} at 3.65 eV, which serves as an estimation of the optical band gap.

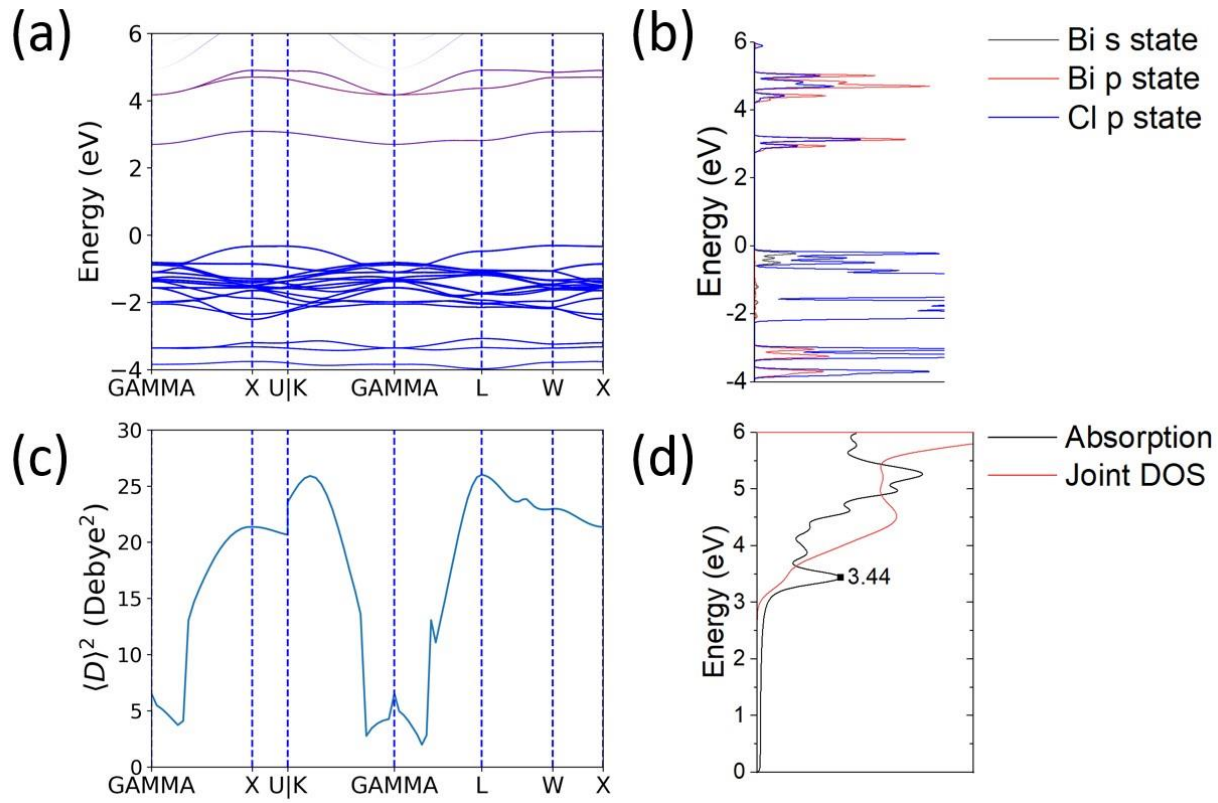

Fig. S1 (a) The band structure and (b) the density of states of $Cs_2NaBiCl_6$ accompanied with (c) the square of electric dipole transition dipole moment and (d) the absorption spectrum and joint DOS. All these data are achieved with the PBE density functional. In (a) and (b), the VBM is set at zero for convenience; PBE underestimates the band gap as 3.01 eV. Black, red and blue represent Bi-*s* state, Bi-*p* state and Cl-*p* state respectively in (a) and (b). It is noted that the energy in (d) has not been corrected for the PBE's underestimation of band gap.

S2a. Formation energy and charge transition (CT) levels. The formation energy of a defect X in the charge state of q is defined as:[14]

$$E^f[X^q] = E_{\text{tot}}[X^q] - E_{\text{tot}}[\text{bulk}] - \sum_i n_i \mu_i + qE_F, \quad \text{(S1)}$$

where $E_{\text{tot}}[X^q]$ and $E_{\text{tot}}[\text{bulk}]$ are the total energies derived from a supercell representing the defect and the pristine host, respectively; n_i is the change in the number of type i atom species, which is added to ($n_i > 0$) and or removed from ($n_i < 0$) the perfect supercell; μ_i is the relative chemical potential for type i atom species and E_F is the electron Fermi energy. *Post hoc* corrections to $E_{\text{tot}}[X^q]$, the total energy of charged defects, were employed and we followed the method proposed by Durrant et al.,[15] where the combination of the Lany-Zunger correction[16,17] due to image charge and the potential alignment between neutral systems has been shown to yield accurate corrections for cubic supercells. The detailed procedures have been given by us previously[5] and are not elaborated here.

The charge transition level (CTL) $X(q_1/q_2)$ for defect X is defined as the Fermi level of the electron reservoir that equilibrates two valence states of energies $E_{\text{tot}}(X^{q1})$ and $E_{\text{tot}}(X^{q2})$ of a defect, i.e.,

$$X(q_1/q_2) = \frac{E_{\text{tot}}(X^{q_1}) - E_{\text{tot}}(X^{q_2})}{q_2 - q_1} \quad \text{(S2)}$$

When $q_1 = q_2+1$, the energy difference of a CTL from the conduction band minimum (CBM), CBM $- X[q_1/(q_1 - 1)]$ and from the valence band maximum (VBM), $X[(q_2 + 1)/q_2]$ − VBM is the energy released when the defect X^{q1} captures an electron from the CBM and X^{q2} captures a hole from the VBM, respectively.

In the calculation of the formation energy of intrinsic defects at different chemical conditions and charge states, the important corrections to the chemical potentials of anion compounds illustrated in Ref. 18 have been included. The detailed chemical potential values adopted in the calculation of defect formation energies are listed in **Table S1**.

Table S1. The chemical potential of each element in $Cs_2NaBiCl_6$ at selected conditions (Energy unit: eV).

	Cl	Bi	Cs	Na
Cl-rich	-0.430	-4.444	-4.225	-3.844
Cl-moderate	-1.200	-2.310	-3.396	-3.015
Cl-poor	-1.969	-0.000	-2.628	-2.246

S2b. Intrinsic defects. The valence band maximum (VBM) is dominated by 3*p* chlorine and bismuth antibonding 6*s* character, whereas the conduction band minimum (CBM) comprises bismuth 6*p* orbitals. Just as for other elpasolites, $Cs_2NaBiCl_6$ can accommodate various intrinsic defects which may influence the host photoluminescence. All four types of Cs, Na, Bi, Cl vacancies, substituting among Bi, Cs and Na, have been taken into consideration. There is one type of Cl vacancy which can potentially be in two charge states (+1,0). All V_{Cl}' are nearest neighbors of bismuth atoms and can have a clear influence on host photoluminescence. Other substitutions are excluded (such as Bi_{Cl}, Cl_{Na}, etc.) due to mismatch of charge or ionic radius. We have not taken interstitials into consideration in our calculations since, unlike tetravalent halide perovskite variants such as Cs_2ZrCl_6 which have enough space for accommodating interstitials, the $Cs_2NaBiCl_6$ crystal is more crowded, and the interstitials are not energy favorable.

The allowed chemical potential region shaped by coexisting conditions of the constituents is mainly characterized by the chemical potential of Cl. Therefore, we select three representative chemical environments to discuss the stability of intrinsic defects, denoted as Cl rich, Cl moderate and Cl poor in **Fig. S2(a),(b),(c)**. For the case of Cl rich, **Fig. S2(a)**, the chemical potentials of Bi, Cs and Na are constrained by $Cs_3Bi_2Cl_9$, Cs_3BiCl_6 and $NaCl_3$ (instead of NaCl due to high chemical potential of Cl). For the case of Cl moderate, **Fig. S2(b)**, the three chemical potentials are constrained in a small range. The chemical environment is constrained by NaCl, $Cs_3Bi_2Cl_9$ and Cs_3BiCl_6. For the case of Cl poor,

Fig. S2(c), the chemical potentials of Bi, Cs and Na are constrained by NaCl, Cs_3BiCl_6 and bismuth metal. The allowed chemical potential regions of Cs, Na and Bi are end points at the extreme oxidizing, **Fig. S2(a)**, and reducing, **Fig. S2(c)**, environments and are marked as a red point in (a) and (c) and represented by a little red triangle for the neutral case, (b). The selection of chemical potential value in this triangle does not have impact on which intrinsic defects are energy favorable. **Fig. S2(d)-(f)** are at the chemical environments represented by these designations in **Fig. S2(a)-(c)**, with the values listed in **Table S1**.

Among all the intrinsic defects we have considered in **Fig. S2(d)-(f)**, the main positive defect species $V_{\mathrm{Cl}}^{\cdot}$ balances with the main negative defect species V_{Na}'in charge under all significant chemical conditions. Other minor defects are positively charged $\mathrm{Bi}_{\mathrm{Na}}^{\cdot\cdot}$ and negatively charged V_{Cs}' and $\mathrm{Cl}_{\mathrm{i}}'$. Although energetically favorable under all chemical conditions, V_{Na}' is located away from the Bi site (Cs and Na are not nearest neighbors of Bi), so that the vacancy has limited influence upon photoluminescence, and we expect that the calculated bismuth excitation and emission energies are only lightly perturbed (just as for the case of V_{Cs}').

S2c. Bi^{3+} ion luminescence and self-trapped exciton (STE)-like excitation states. The VBM is composed of the 3*p* orbitals of Cl and partly of the 6*s* orbitals of Bi (**Fig. S1(a),(b)**), which indicates that Bi^{3+} photoluminescence can be contributed by (i) the $6s^2 \rightarrow 6s6p$ ($^1S_0 \rightarrow {}^3P_{0,1}$) transition or (ii) the charge transfer transition between Cl-3*p* and Bi-6*p*.

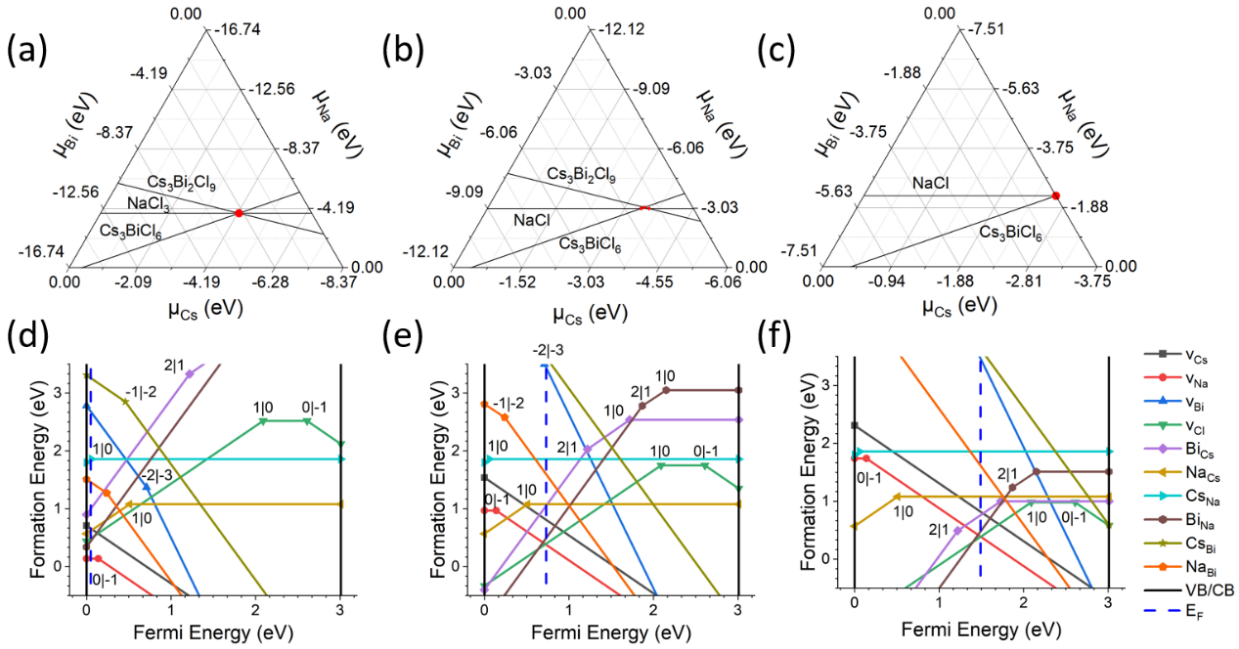

Fig. S2 The cross section of allowed ranges of elemental chemical potentials to sustain $Cs_2NaBiCl_6$ at Cl rich (a), Cl moderate (b) and Cl poor (c) conditions, and the formation energies of defects calculated *via* the PBE method under corresponding chemical environments (d-f). The symbols E_F, CB and VB in the legend represent the Fermi energy determined by charge neutrality, and the conduction and valence bands, and the two integers such as "0|-1" mark the place where the valence of the defect switches from 0 (high) to -1 (low) as the Fermi energy increases. The relative chemical potential of Cl is fixed at -0.43 eV, -1.20 eV and -1.97 eV in (a), (b) and (c), respectively. It is noted that V'_{Na} and $V^{\cdot}_{Cl}$ may offer shallow hole and electron traps to form V^{x}_{Na} and V'_{Cl}, calculated at ~0.1 eV and ~0.35 eV, respectively.

In the first case (i), for the $Cs_2NaBiCl_6$ host, there are two potential transitions, which are the $6s^2 \rightarrow 6s6p$ transition of a single Bi^{3+} ion (**Fig. S3(a)-(c)**), or a Bi-pair inter-valence charge transfer (IVCT) transition (**Fig. S3(d)**). Just as for the cases of bismuth doped in double perovskites, such as in the elpasolite Cs_2NaYCl_6,[5,19] the configuration coordinate (CC) curve of the $6s6p$ state of a single Bi^{3+} ion

is very flat, and the excitation can be readily ionized. Figs. S3(a) and (b) show the CC curves for transitions of single Bi^{3+} ions adjacent to chlorine and sodium vacancies, respectively. In emission, the V'_{Na} STE comprises a hole on several Bi 6*s* or Cl 3*p* orbitals, with an electron spread over Bi 6*p* orbitals. The $V_{\dot{C}l}$ STE $[BiCl_5]^{2+}$ is envisioned as an electron on a Bi^{3+} ion (forming Bi^{2+}) and a hole spread out on many Bi 6*s* and Cl 3*p* orbitals. Its value in **Table 1** of the manuscript may be underestimated by ~0.4 eV.

Fig. S3(d)-(f) involve transitions with more than one Bi^{3+} ion. **Fig. S3(d)** displays the CC diagram for an IVCT transition between bismuth ions. The distance between two adjacent Bi^{3+} ions is large (7.64 Å) and this hinders Bi - Bi pair CT luminescence. The pair transition between a Bi^{3+} ion with a hole polaron in the excited state and an adjacent bismuth ion occupying the sodium site, with an electron, is shown in **Fig. S3(e)**. The bismuth pair can emit. From the CC curve connecting the single Bi^{3+} ion and the Bi^{3+} pair excited state [**Fig. S3(f)**], there is a 0.10 eV small barrier and a 0.24 eV energy decrease for the single 6*s*6*p* excited state relaxing to the pair IVCT excited state. The calculated excitation and emission energies of the above centres are listed in **Table 1** of the manuscript.

For the second case above (ii), we also calculated the Cl_2^- type STE transition in $Cs_2NaBiCl_6$, which has been reported in tetravalent perovskites like Cs_2HfCl_6.[20,21] Two of the six Cl^- ligand ions around Bi^{3+} come closer together and form a Cl_2^- molecule-like structure which accommodates the hole of the STE (instead of being on Bi) and the electron of the STE is located on Bi^{3+}. We find that the energy of this STE state is higher than the *sp* excited state on a single Bi^{3+} ion, which means that the Cl_2^- STE state is unlikely to luminesce.

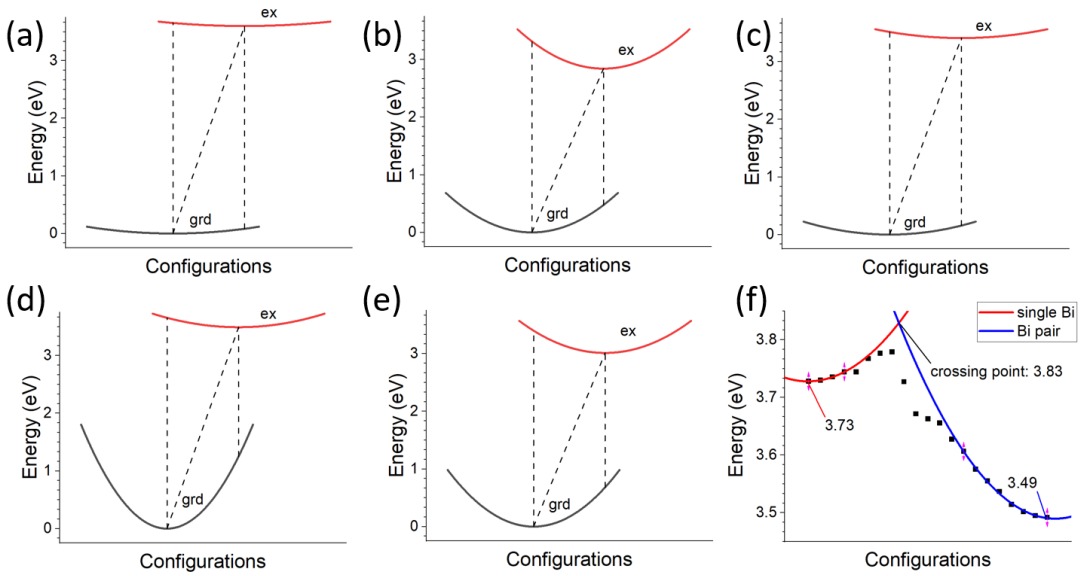

Fig. S3 The CC diagrams for various scenarios. (a) the CC curve for a single Bi^{3+} ion in $Cs_2NaBiCl_6$; (b) Bi^{3+} ($6s^2 \rightarrow 6s6p$) with the nearest $V_{Cl}^{\cdot}$; (c) Bi^{3+} ($6s^2 \rightarrow 6s6p$) with the nearest V_{Na}'; (d) the CC curve for a pair of Bi^{3+} ions in $Cs_2NaBiCl_6$ (like $2Bi^{3+} \rightarrow Bi^{2+} + Bi^{4+}$ (Bi_{Bi}' + $Bi_{Bi}^{\cdot}$); (e) pair transition between Bi^{3+} and $Bi_{Na}^{\cdot\cdot}$; (f) the CC diagram linking Bi^{3+} and bismuth-pair excited states in $Cs_2NaBiCl_6$. In each case, the energies in these diagrams are relative to the ground state and the curves are fitted by quadratic functions. Curve (f) is calculated in detail (black points). The barrier between the excited state of Bi^{3+}(1) ($6s6p$ $^3P_0$, $6s^2$ $^1S_0$) and the pair ($6s$ $^2S_{1/2}$, $6s^26p$ $^2P_{1/2}$) is calculated along the two equilibrium configurations. The actual lowest barrier may be much smaller. Vertical dashed lines represent vertical electronic transitions whilst the diagonal dashed line represents the zero-phonon line location. The zero-point vibrational energies are neglected.

S2d. Calculations involving other defects. After including O-related defects together with intrinsic ones, we find that O-related defects are actually not important. It is noted that the chemical potential of O is constrained by $CsClO_4$ in the Cl rich condition (**Fig. S4(a)**), BiClO in the Cl moderate

condition (**Fig. S4(b)**) and the Cl poor condition (**Fig. S4(c)**). The CTLs of O-related defects are plotted in dashed lines.

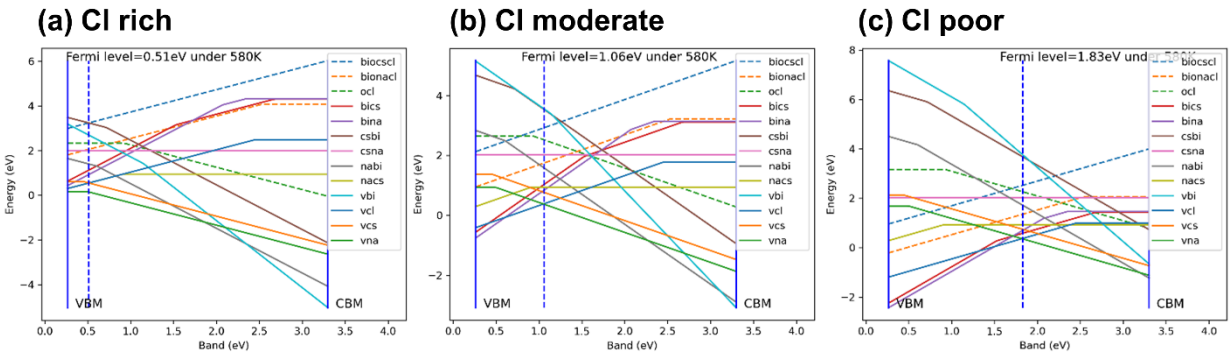

Fig. S4 The formation energies of defects calculated *via* the PBE method under the chemical environments of $Cs_2NaBiCl_6$ at Cl rich (a), Cl moderate (b) and Cl poor (c) conditions.

To show the relative importance of the three O-related defects more clearly, their relative formation energies are plotted in **Fig. S5**. Here the change in chemical potential of O element only shifts the formation energies of all the three O-related defects uniformly and so has been set the same as the chemical potential of Cl for simplicity. The structures of two dominant O-related defects are plotted in **Fig. S6** (O'_{Cl}) and **Fig. S7** ($Bi''_{Na} + O'_{Cl}$).

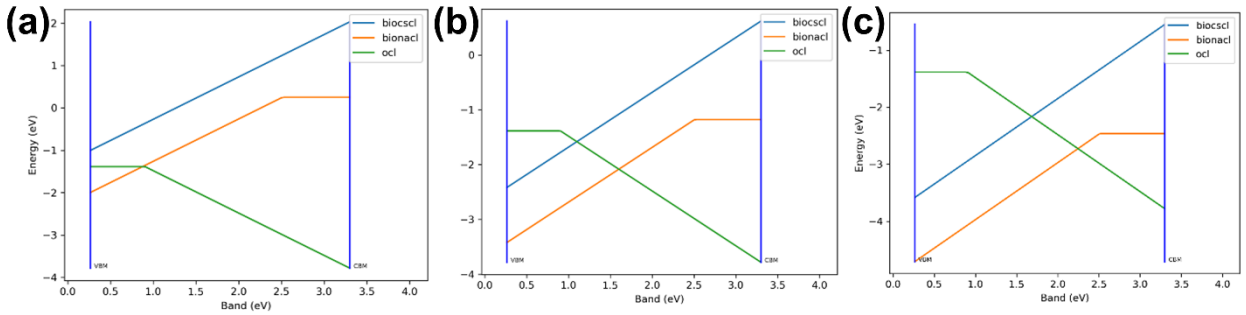

Fig. S5 Band gap energy diagrams for O-included defects for (a) Cl rich, (b) Cl moderate and (c) Cl poor conditions. In this figure bionacl and biocscl refer to Bi_{Na}-O_{Cl}, and Bi_{Cs}-O_{Cl}, respectively, and ocl to O_{Cl}^{-} . The $Bi_{Na}^{\cdot\cdot} + O_{Cl}^{\prime}$ complex and O_{Cl}^{-} are the dominant defects among all the considered O-included defects.

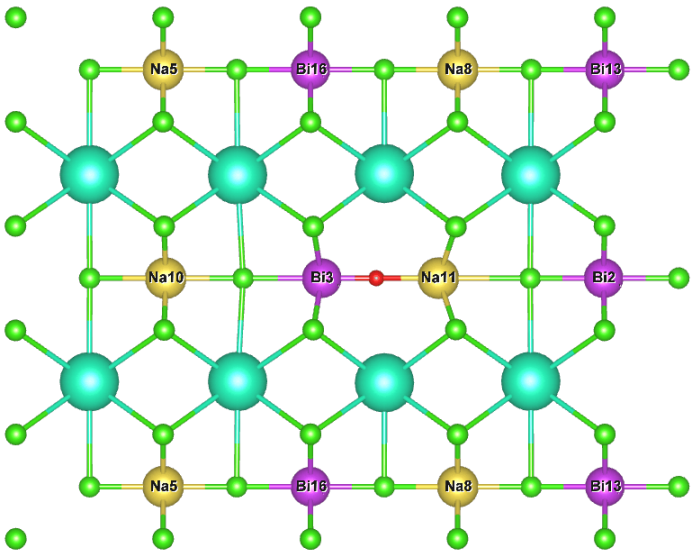

Fig. S6 Structure of the $O_{Cl}^{\prime}$ defect (O marked in red) in $Cs_2NaBiCl_6$ crystal viewed from (110) direction. The red spot is O at the Cl site and Bi3 is the nearest Bi atom at its own lattice site. This defect can also be viewed as Bi_{Bi}^{x} -$O_{Cl}^{\prime}$, which produces the $6s^2 \leftrightarrow 6s6p$ transition of calculated lowest absorption at 3.58 eV and emission at 1.73 eV.

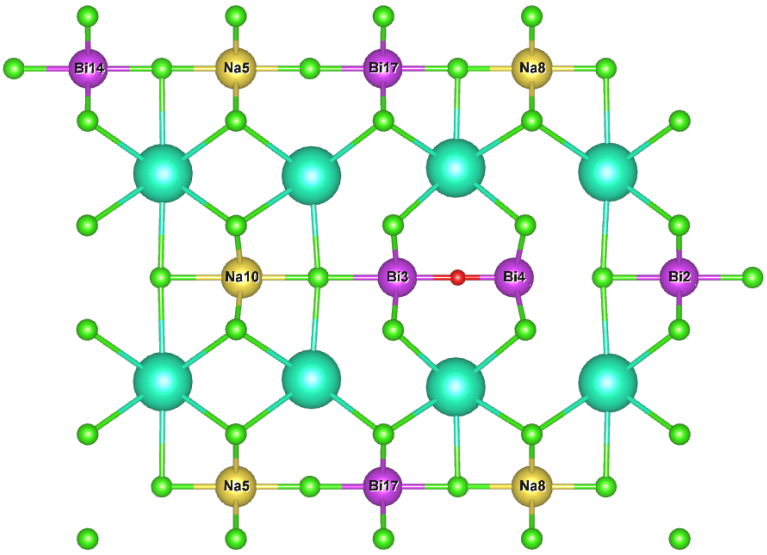

Fig. S7 Structure of the $Bi_{Na}^{\cdot\cdot} + O_{Cl}'$ defect in $Cs_2NaBiCl_6$ crystal viewed from (110) direction. The red spot is O at the Cl site and Bi4 is the Bi atom at the Na site. The defect can also be viewed as $Bi_{Bi}^{x} - O_{Cl}' - Bi_{Na}^{\cdot\cdot}$ that contains two active Bi^{3+} ions, which produces an IVCT transition [$2Bi^{3+} \rightarrow Bi^{2+} + Bi^{4+}$] with calculated lowest absorption at 3.22 eV and emission at 2.48 eV.

We have also calculated the energies for other defects which are not dominant in $Cs_2NaBiCl_6$, including V_{Cs}', Bi_{Cs}^{x} (i.e., Bi^{+} at the Cs site), and $Bi_{Cs}^{\cdot\cdot}$. In the former case, the emission is likely to be quenched. For Bi_{Cs}^{x}, the excitation is calculated at 2.21 eV (561 nm) and the emission is calculated at 1.57 eV (790 nm) or estimated between 1.5-1.8 eV. In the latter case, $Bi_{Cs}^{\cdot\cdot}$, the transition is: $2Bi^{3+} \rightarrow Bi^{2+} + Bi^{4+}$, or explicitly $(Bi_{Cs})^{2+} + Bi_{Bi} \rightarrow (Bi_{Cs})^{+} + Bi_{Bi}^{+}$, (**Fig. S6**). The excitation energy is calculated as 3.49 eV whereas the emission is at 1.34 eV (PBE0 and scan) or 1.17 eV (HSE06), i.e. 925 nm – 1060 nm. The excitation and emission energies are summarized in **Table 1** of the manuscript.

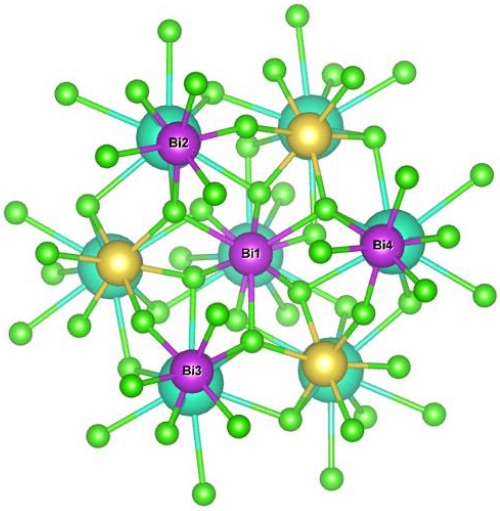

Fig. S8 View along the C_3 axis after Bi_1 substitutes a Cs ion. Bi_1 and Bi_5 are on that axis, and Bi_5 is nearer than other three bismuth ions by 1 Å (4.00 Å and 5.07 Å). The transition is actually $s(Bi_2,Bi_3,Bi_4) \rightarrow p(Bi_1)$.

We have also performed calculations for the two Cs-Bi-Cl compounds Cs_3BiCl_6 and $Cs_3Bi_2Cl_9$ which may occur in the synthesis of $Cs_2NaBiCl_6$. Using the PBE0 ($\alpha = 0.32$) calculation, in $Cs_3Bi_2Cl_9$, the bismuth pair emission is calculated at 2.42 eV (512 nm); the bismuth pair with a Cl vacancy emission is calculated at 1.40/0.88 eV (886/1409 nm) for two different Cl sites. In Cs_3BiCl_6, the Bi^{3+} (*s*-*p*) emission is calculated at 2.35 eV (528 nm).

S3. Equations

Jorgensen's equation for predicting charge transfer transition energy, E_{CT} (in cm^{-1}):[22]

$$E_{CT} = 30000(x_{opt}(X) - x_{opt}(M)] \quad \text{(S3)}$$

where $x_{opt}(X)$ and $x_{opt}(M)$ are the optical electronegativities of the halide and metal in the relevant oxidation states, respectively.

For measurement of average lifetime from biexponential decay, the intensity average lifetime, τ_{av}, is given by:

$$\tau_{av} = \frac{\sum_i A_i \tau_i^2}{\sum_i A_i \tau_i} \quad \text{(S4)}$$

where the A_i are the coefficients of τ_i and i = 1,2. The amplitude average lifetime is given by:

$$\tau'_{av} = \frac{\sum_i A_i \tau_i}{\sum_i A_i} \quad \text{(S5)}$$

The simplest equation for the temperature dependence of lifetime using a barrier model with activation energy E_{act} (cm^{-1}) is:

$$\tau(T) = \frac{1}{k_r + G\exp(-\frac{E_{act}}{0.69503T})} \quad \text{(S6)}$$

where k_r is the radiative lifetime and G is a constant.

For a two-barrier model, we have used the simple equation:

$$\tau(T) = \frac{1}{k_1 + G_1\exp(-\frac{E_{act,1}}{0.69503T})} + \frac{1}{G_2\exp(-\frac{E_{act,2}}{0.69503T})} \quad \text{(S7)}$$

The full width at half-maximum (FWHM, Γ) of a Pekarian curve representing an absorption transition approximates a Gaussian shape at large values of the Huang-Rhys parameter S and the temperature dependence is given by:

$$\Gamma(T) = 2.36\hbar\omega S^{1/2}\sqrt{\coth\frac{\hbar\omega}{2kT}} \quad \text{(S8)}$$

where $\hbar\omega$ represents the vibrational mode frequency and k is the Boltzmann constant.

The initial rise method calculates activation energy, which is the depth of a trap, by fitting the initial part of a glow curve and is applicable for any order of kinetics but can only be used for non-

overlapping glow curves, where the peak rises from the baseline. The activation energy E is the slope of the plot of ln(I) versus 1/kT , where I is intensity, k is the Boltzmann constant and T is temperature.[23]

$$\ln(I) = \ln(csn_0) - \frac{E}{kT} \quad \text{(S9)}$$

Where n_0 is the initial trap number, s is a frequency factor, and c is a constant related to luminescence efficiency.

The Kitis et al. equation for general order kinetics glow curves can be used to find activation energy E, :[23]

$$I(T) = I_M b^{\frac{b}{b-1}} \exp\left(\frac{E}{kT}\frac{T-T_M}{T_M}\right)\left[1 + (b-1)\frac{2kT_M}{E} + (b-1)(1-\frac{2kT}{E})(\frac{T^2}{T_M^2}\exp\left(\frac{E}{kT}\frac{T-T_M}{T_M}\right))\right]^{\frac{-b}{b-1}} \quad \text{(S10)}$$

where $I(T)$ is the intensity at temperature T, b is the kinetics order, T_M is the temperature at which intensity is a maximum. The plot of $I(T)$ versus T can be fitted by the two parameters b and E since T_M and I_M are known.

S4. XPS spectra

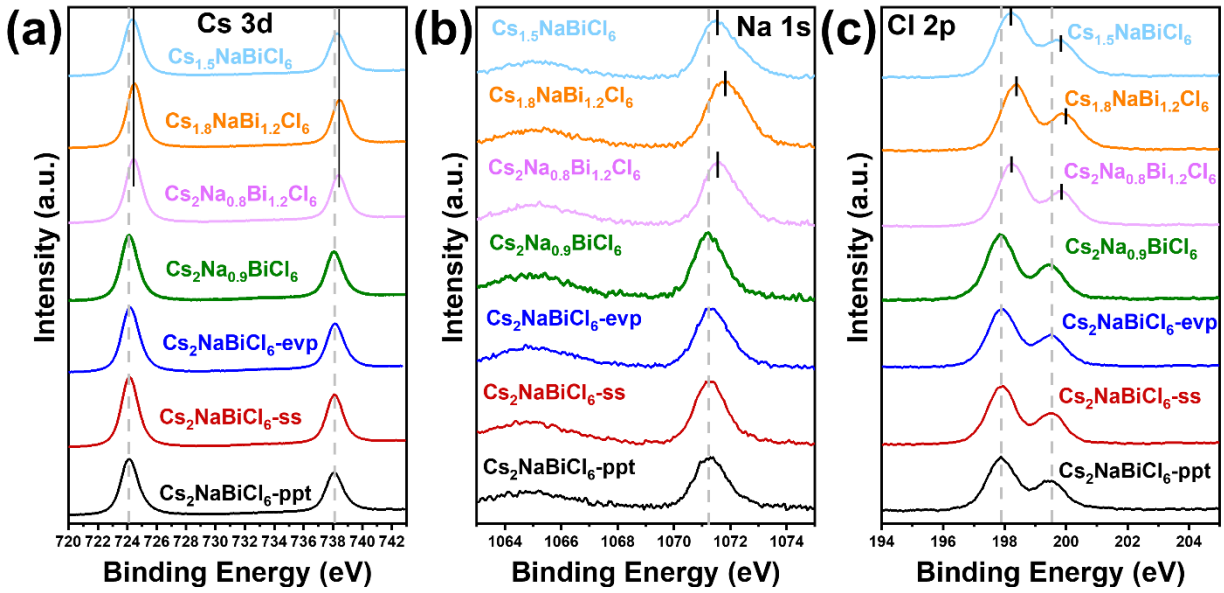

Fig. S9 The Cs 3d (a), Na 1s (b), and Cl 2p (c) XPS spectra for $Cs_2NaBiCl_6$ and nonstoichiometric samples.

S5. Absorption, excitation and emission spectra and emission decay curves: blue, green and red emission

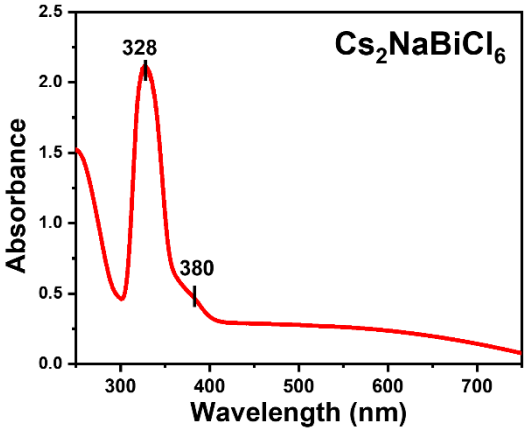

Fig. S10 Room temperature UV-vis absorption spectrum of a $Cs_2NaBiCl_6$-NaCl pressed disc.

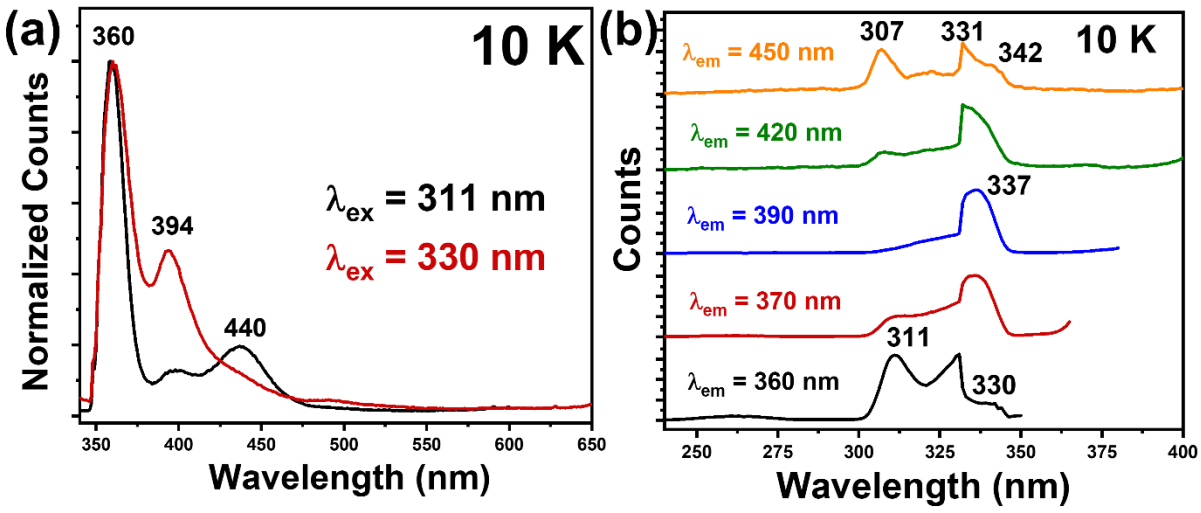

Fig. S11 (a) Emission and (b) excitation spectra of $Cs_2NaBiCl_6$ evp sample at 10 K.

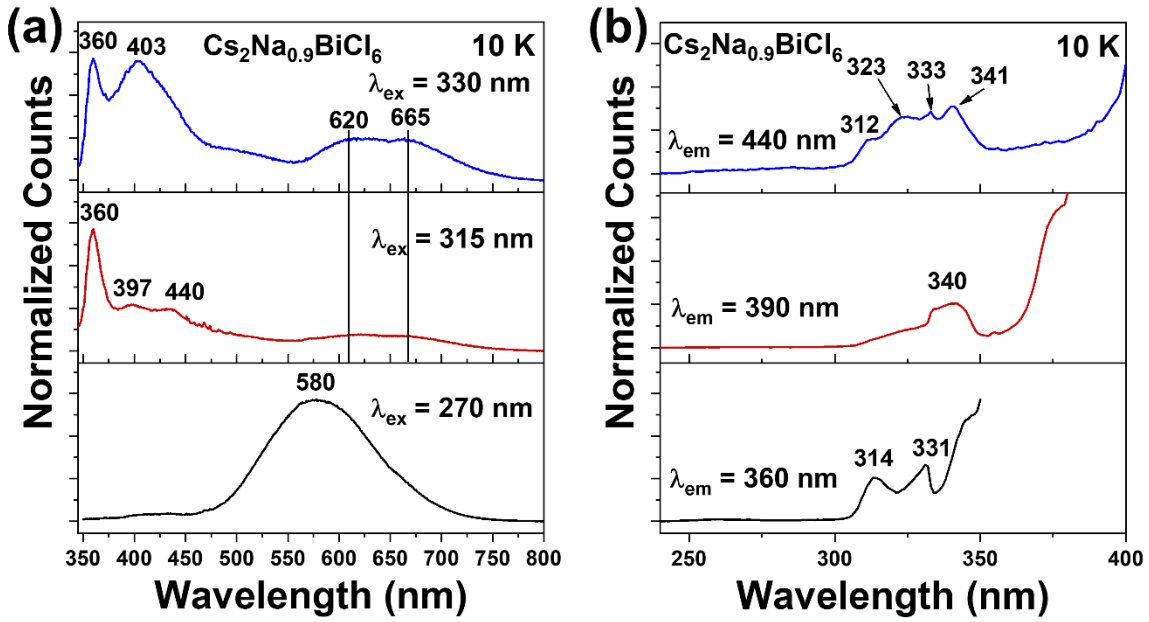

Fig. S12 10 K emission and excitation spectra of sodium-depleted samples prepared by evp method.

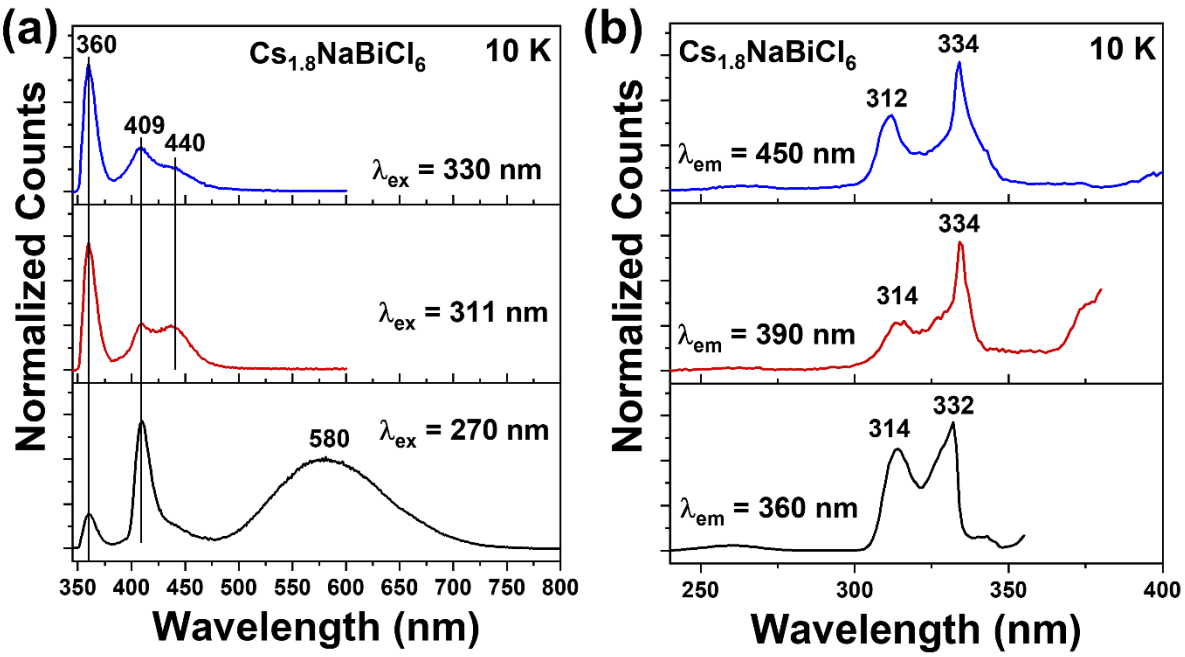

Fig. S13 10 K emission and excitation spectra of caesium-depleted samples prepared by evp method.

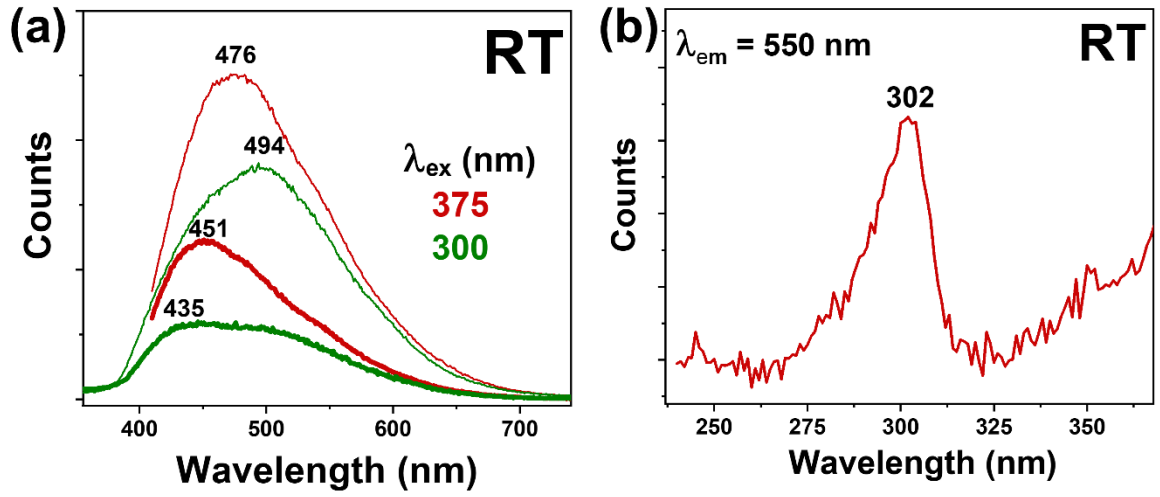

Fig. S14 (a) Emission (thin lines) and (b) excitation spectra of $Cs_2NaBiCl_6$ NPs at RT. The thick lines in (a) represent the same material after storage for 18 d in a dry box.

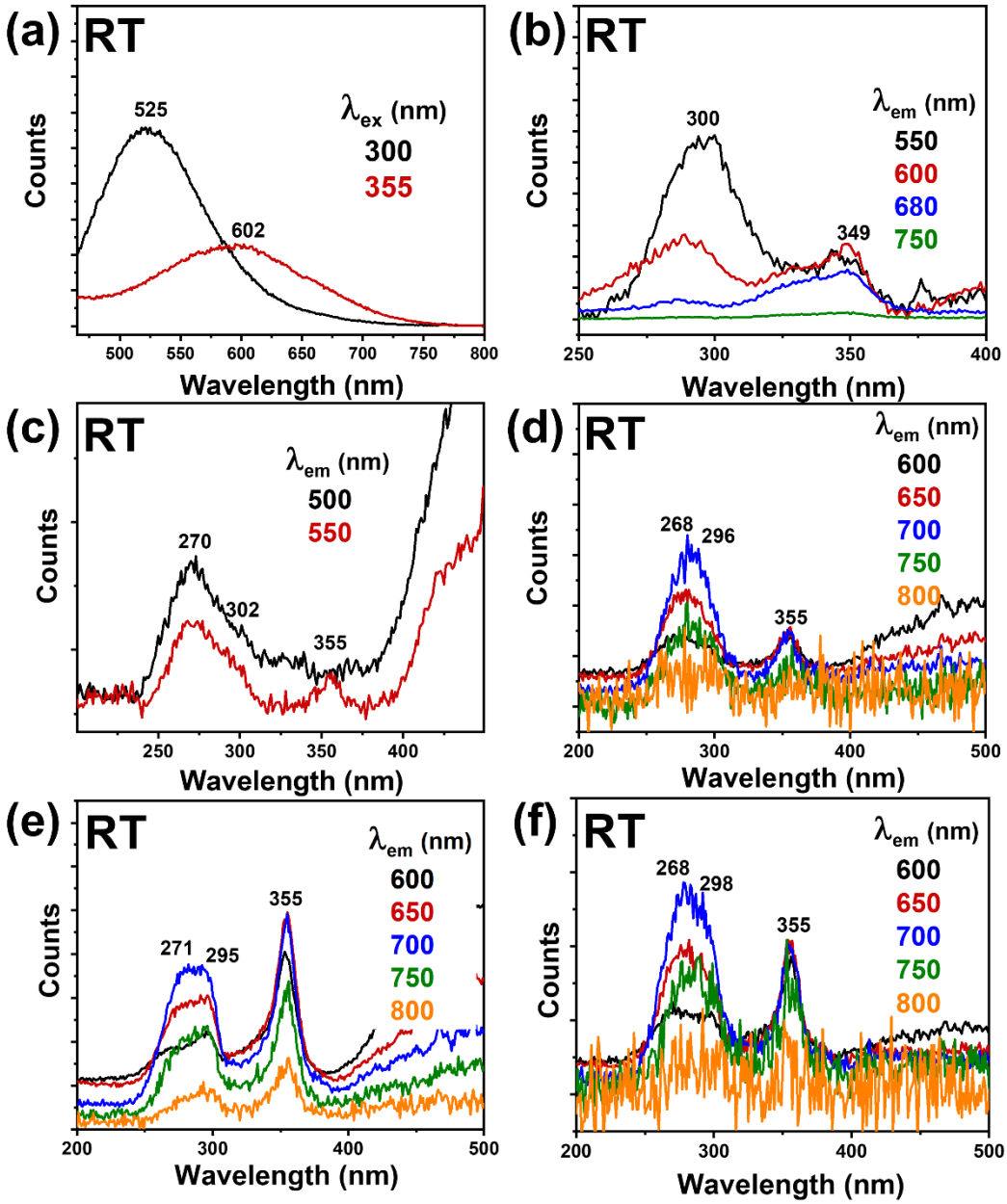

Fig. S15 (a) RT emission and (b)-(d) excitation spectra of $Cs_2NaBiCl_6$ samples prepared by ss method (without nujol) with drying at 120 ^oC. RT excitation spectra of (e) evp: nujol, DCl and (f) evp: DCl samples.

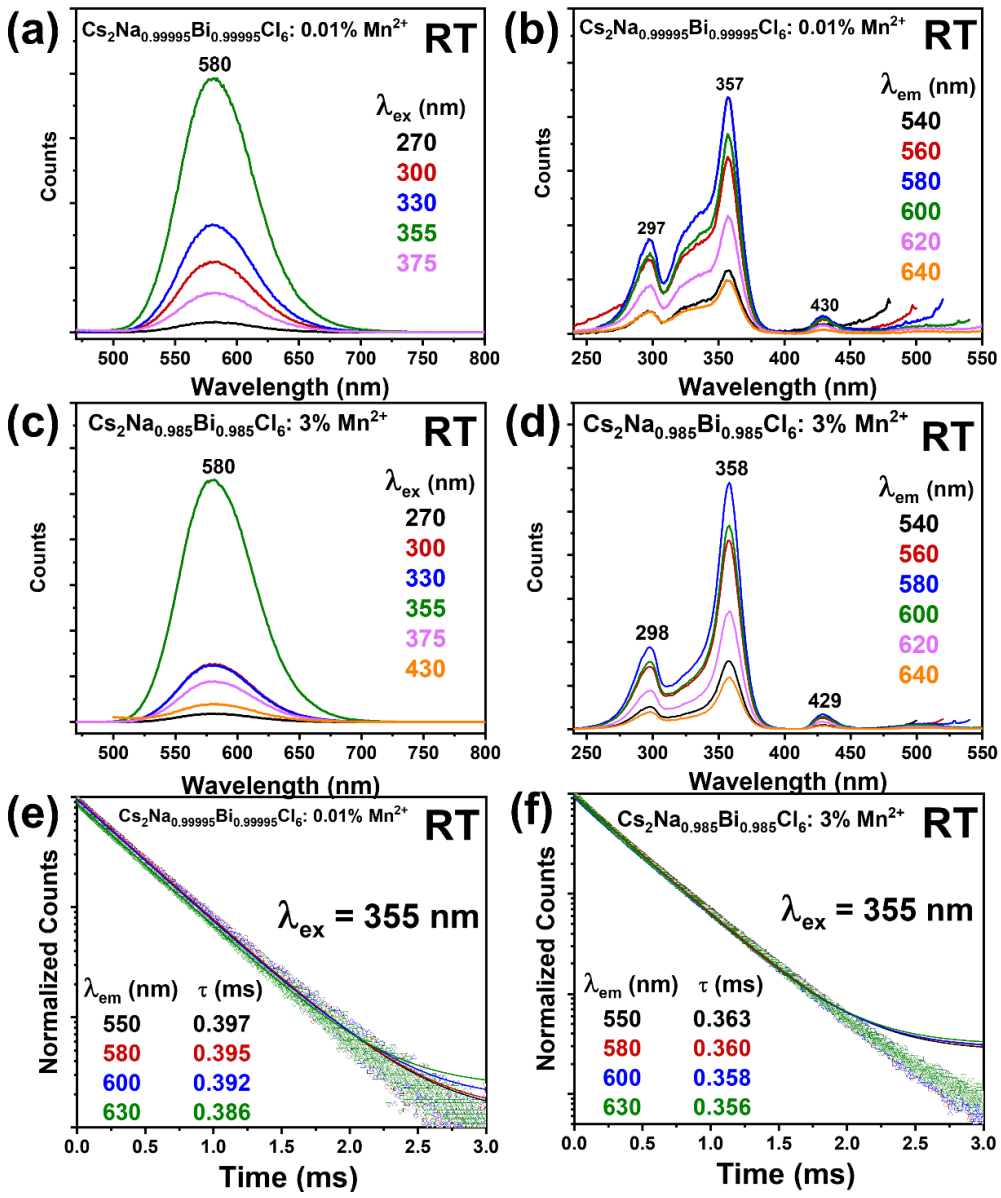

Fig. S16 Spectra (a)-(d) and decay curves (e), (f) of Mn-doped $Cs_2NaBiCl_6$ samples at room temperature.

Table S2. Monoexponential lifetimes of Mn-doped $Cs_2NaBiCl_6$ samples at RT.

λ_{em} (nm)	0.01 % Mn^{2+}		3 % Mn^{2+}	
	Lifetime (ms)	R_{adj}^2	Lifetime (ms)	R_{adj}^2
550	0.397±4E-4	0.9995	0.364±3E-4	0.9997
580	0.395±3E-4	0.9996	0.360±3E-4	0.9997
600	0.392±4E-4	0.9995	0.358±3E-4	0.9997
630	0.386±6E-4	0.9990	0.356±3E-4	0.9997

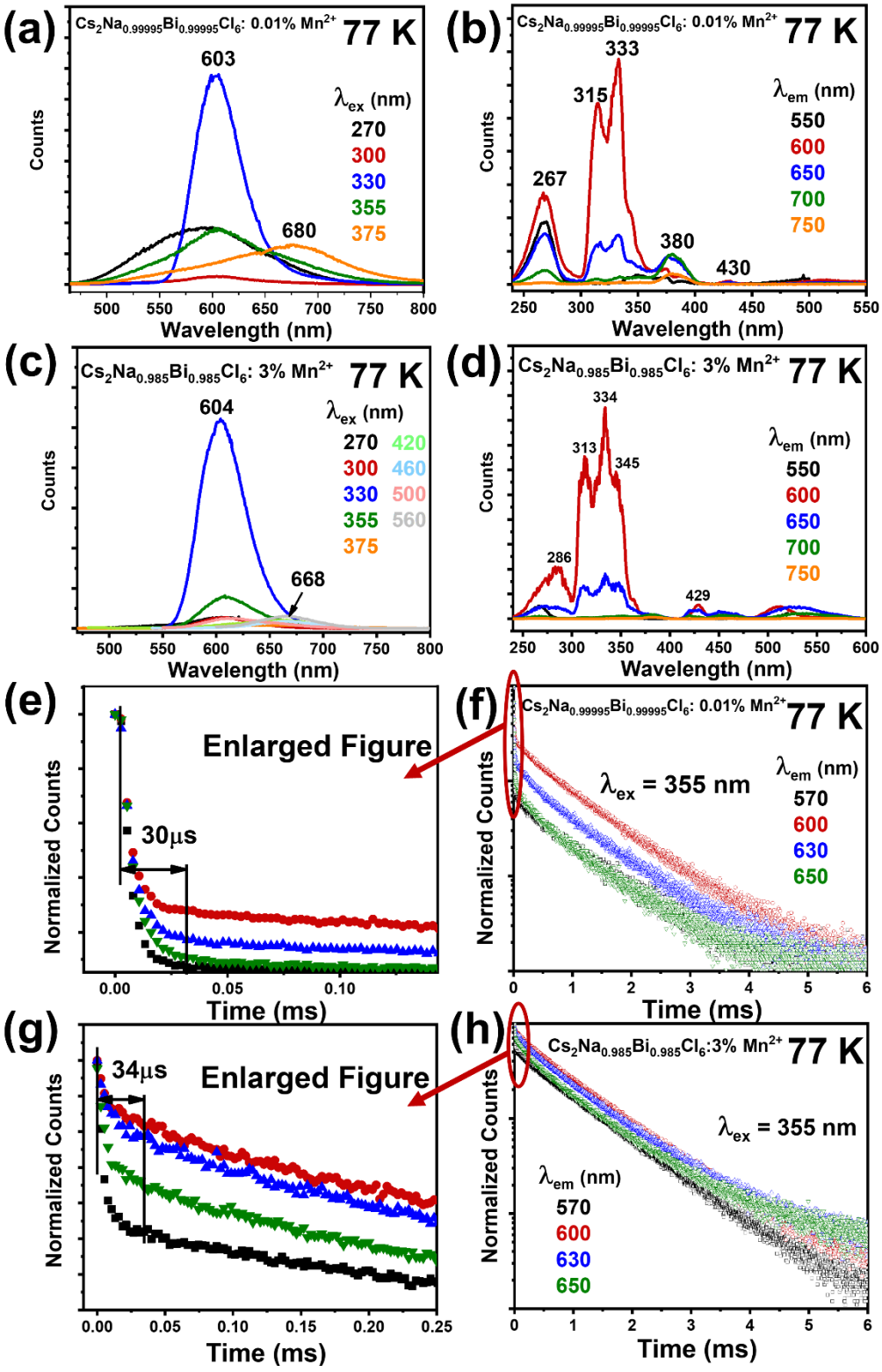

Fig. S17 Spectra (a)-(d) and decay curves (e)-(h) of Mn-doped $Cs_2NaBiCl_6$ samples at 77 K.

Table S3. Biexponential lifetimes of Mn-doped $Cs_2NaBiCl_6$ samples at 77 K.

λ_{em} (nm)	0.01 % Mn^{2+}			3 % Mn^{2+}		
	τ_1 (µs)	τ_2(ms)	R_{adj}^2	τ_1 (µs)	τ_2(ms)	R_{adj}^2
570	6.77±0.05	0.86±0.02	0.9756	6.1±0.1	0.87±0.0	0.9985
600	7.45±0.07	0.82±0.00	0.9940	123±3	0.93±0.00	0.9993
630	8.1±0.06	0.73±0.00	0.9907	135±3	0.91±0.00	0.9990
650	8.3±0.06	0.68±0.01	0.9847	89±2	0.84±0.00	0.9972

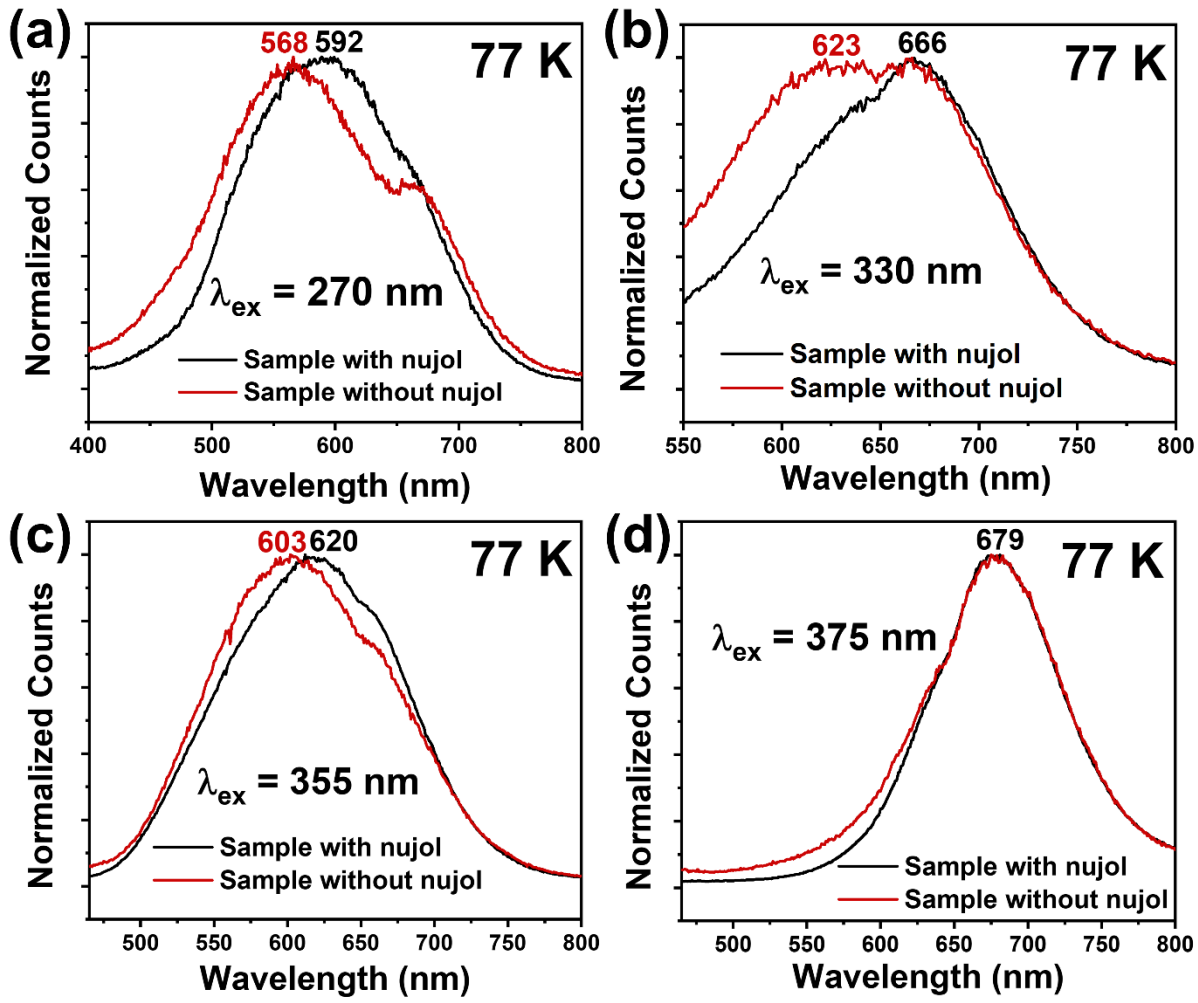

Fig. S18 Comparison of evp and evp:nujol sample emission at 77K.

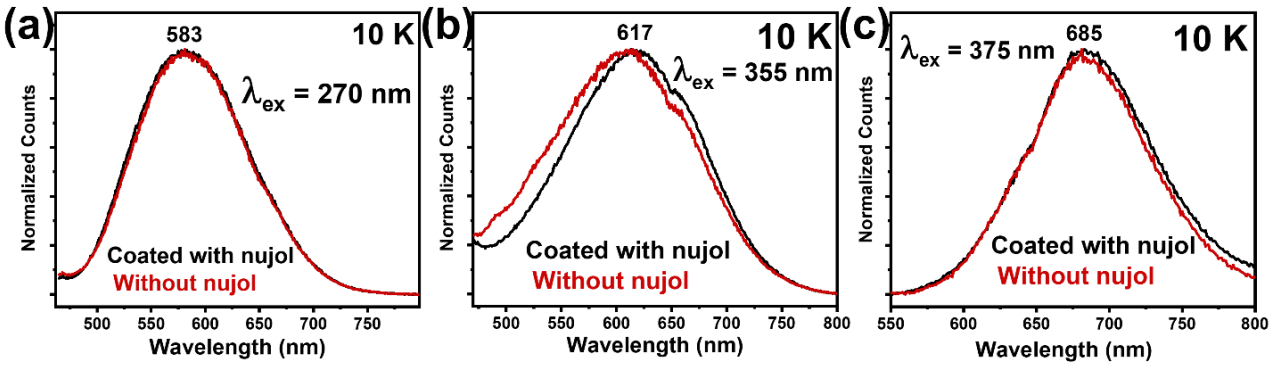

Fig. S19 Repeated synthesis from Fig. S18 and comparison of evp and evp:nujol sample emission at 10 K.

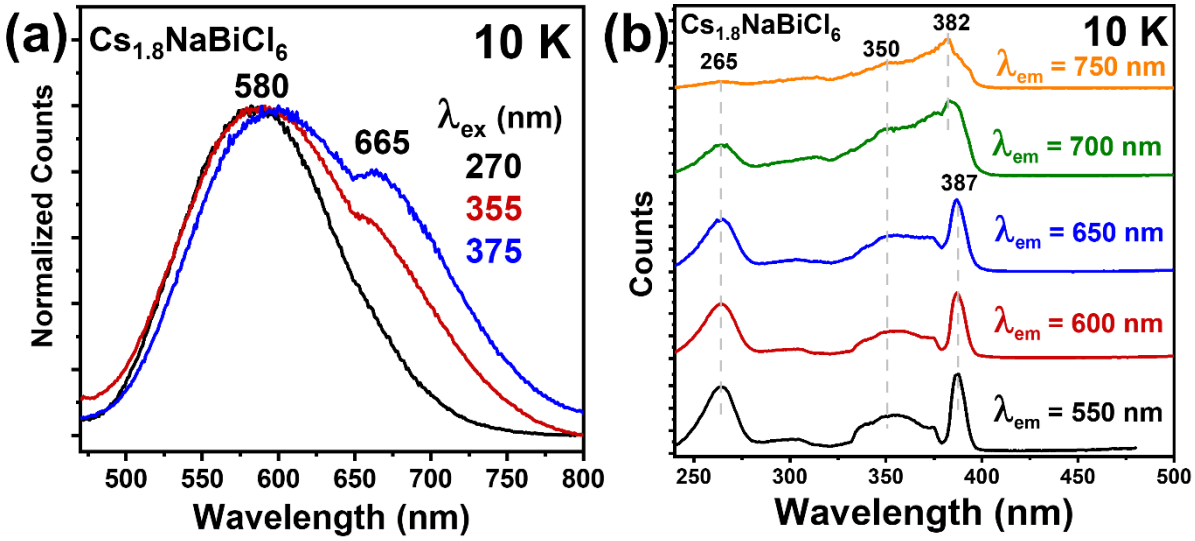

Fig. S20 Red emission and excitation spectra of caesium depleted samples, $Cs_{1.8}NaBiCl_6$, prepared by evp method at 10 K.

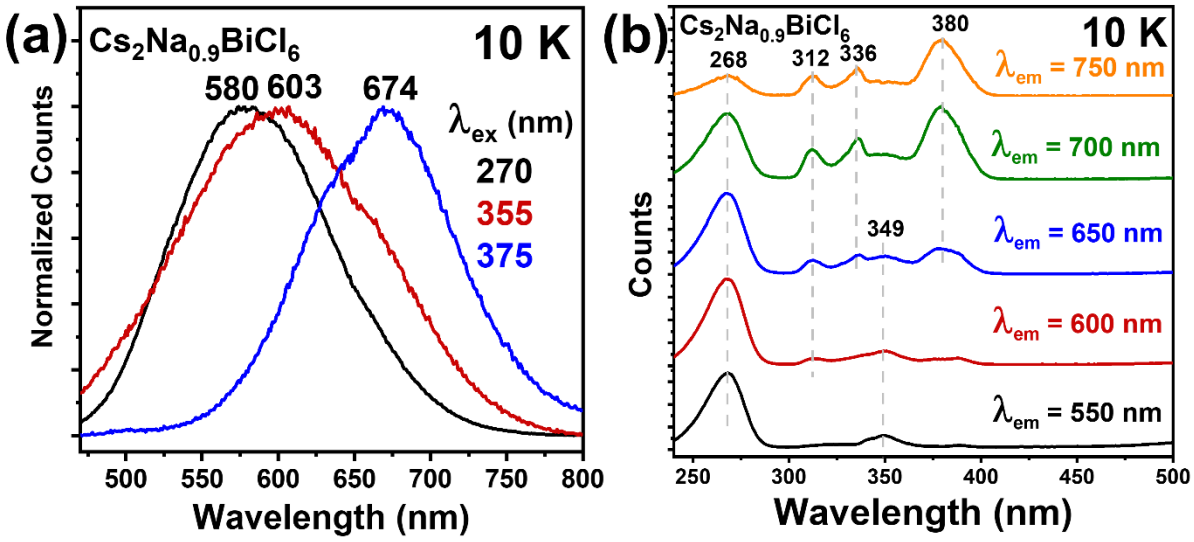

Fig. S21 Red emission and excitation spectra of sodium depleted samples, $Cs_2Na_{0.9}BiCl_6$, prepared by evp method at 10 K.

Table S4. Biexponential lifetime fits for red emission of $Cs_2NaBiCl_6$ evp sample at 77 K, **Fig. 6(a)** in manuscript.

λ_{em} (nm)	A_1	τ_1	A_2	τ_2	R_{adj}^2
550	0.33	2.12±0.06	0.66	4.86±0.05	0.9999
600	0.37	2.41±0.06	0.62	5.46±0.07	0.9999
650	0.40	2.59±0.05	0.59	6.28±0.08	0.9999
700	0.34	2.46±0.05	0.65	7.00±0.07	0.9999

Table S5. Biexponential lifetime fits for red emission of $Cs_2NaBiCl_6$ evp sample at 10 K, **Fig. 6(c)** in manuscript.

λ_{em} (nm)	A_1	τ_1	A_2	τ_2	R_{adj}^2
550	0.39	10.9±0.2	0.56	34.6±0.5	0.9998
600	0.42	11.5±0.2	0.56	31.0±0.4	0.9999
650	0.43	11.6±0.2	0.55	30.2±0.4	0.9999
700	0.41	11.5±0.2	0.57	31.3±0.3	0.9999

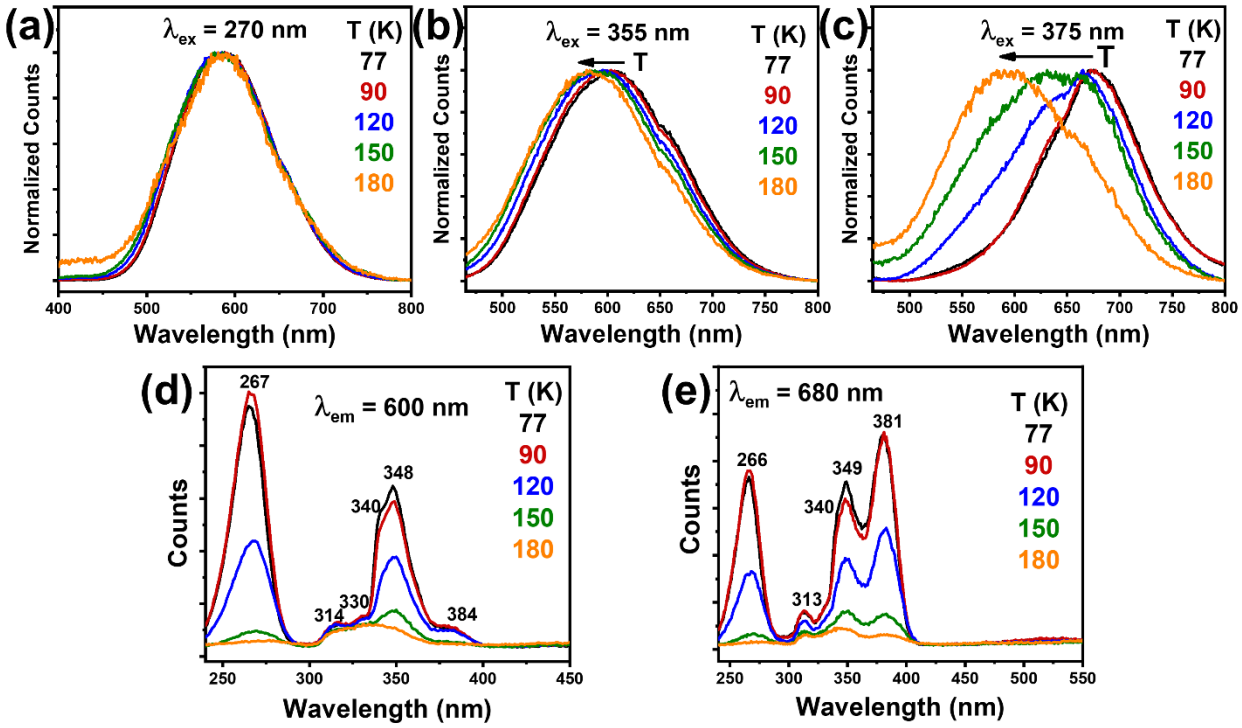

Fig. S22 Temperature dependence of red emission (a)-(c) and excitation spectra (d),(e).

S6. Temperature dependence of red emission

Krasnikov et al.[24] have fitted the dynamics of bismuth emission with a three excited level model with 7 or 8 parameters, ignoring changes in nonradiative rates with temperature but accounting for thermalization. We fitted one of their data for the temperature dependence of lifetime with a simple two barrier model with 5 parameters (Eq. S7) and obtained similar activation energies. Hence, we fitted the variable temperature monoexponential lifetime and intensity data of Pelle et al.[25] for 620 nm emission under 253.7 nm excitation (which are similar to our more limited data for 270 nm excitation) with this model and obtained activation energies of ~0.12 eV and ~3 meV (**Fig. S23**).

Under 337.1 nm excitation, biexponential decay was observed by Pelle et al.[25] for the red emission band, with fast and slow components in the microsecond regime, just as we observe under 355 nm excitation. Our fits of the two barrier model to these temperature-dependent lifetimes are not very good and give activation energies of 0.05 eV, 1 meV (fast) and 0.2 eV, 5 meV (slow), respectively (**Fig. S24**). Krasnikov et al. associated the activation energies to (i) the splitting of the triplet excited state and (ii) another excited state, not discussed. In conclusion, the activation energies are in the order of 0.05-0.2 eV and 3±2 meV.

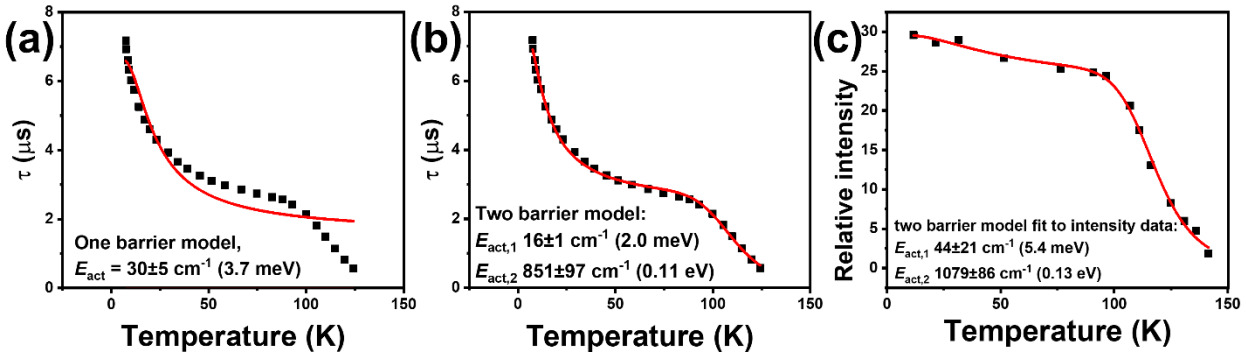

Fig. S23 (a), (b) Fit of lifetime-temperature data of Pelle et al.[29] for 253.7 nm excited emission at 620 nm with one and two barrier models. The measured lifetimes are in reasonable agreement with our results using 270 nm excitation of about 5 µs at nominal 10 K. (c) Fit using the published intensity data.

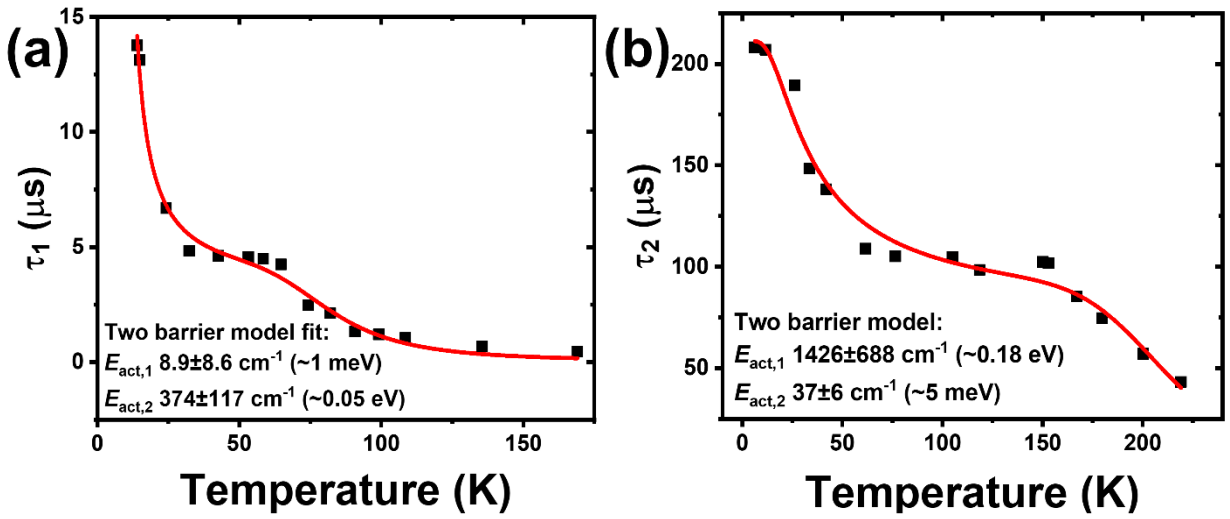

Fig. S24 Fit of lifetime-temperature data of Pelle et al.[25] for the (a) fast and (b) slow components of the total red emission, excited by 337.1 nm, with a two barrier model. The measured lifetimes are similar to our results using 355 nm excitation of about 11 μs and 30 μs at nominal 10 K, but with the latter being rather smaller than in (b). However, the measurement wavelength range is different.

S7. NIR and IR emission

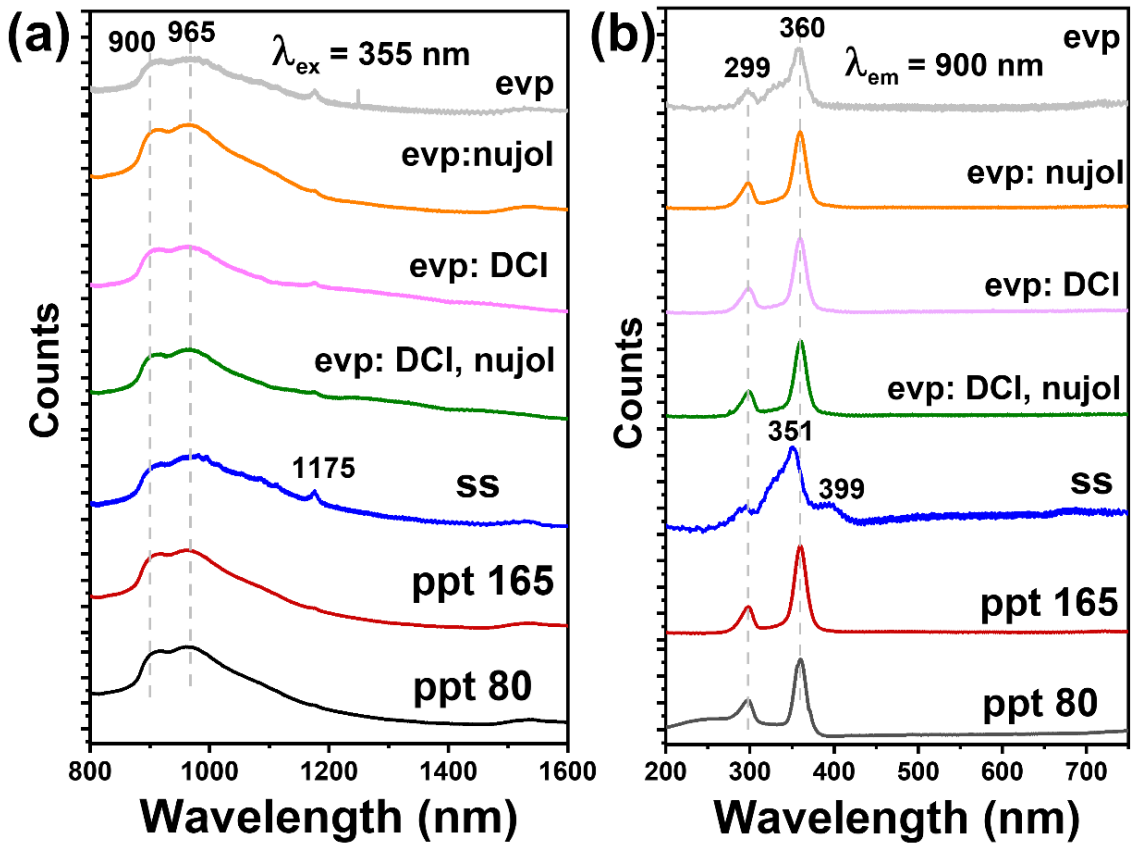

Fig. S25 (a) 355 nm excited RT NIR emission spectra of samples prepared as shown. (b) RT excitation spectra of λ_{em} = 850 nm, except shown otherwise.

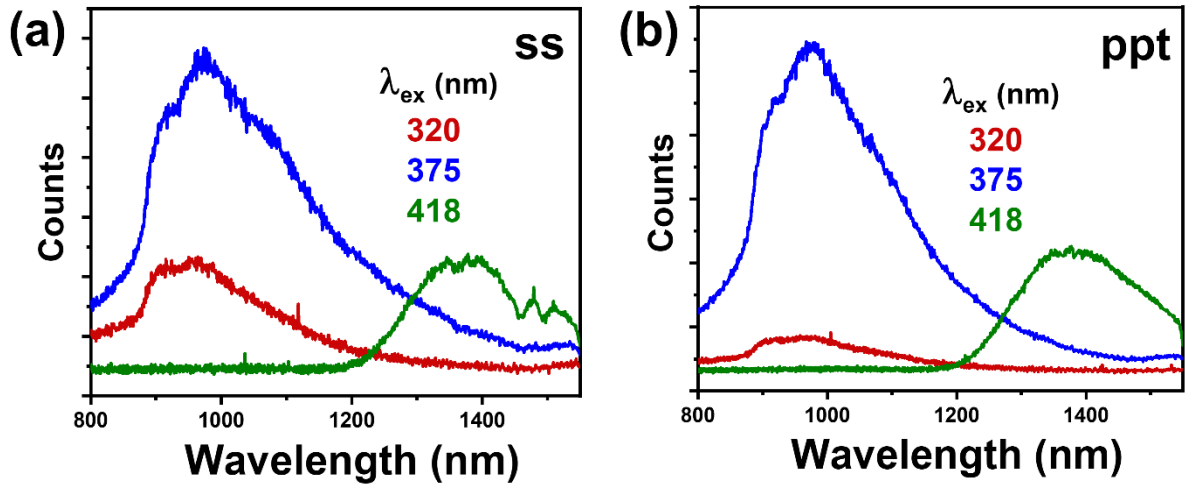

Fig. S26 77 K emission spectra using longer excitation wavelengths than in Fig. S25. The ppt method introduces less water into the product so the emission band is more clearly observed due to less self-absorption.

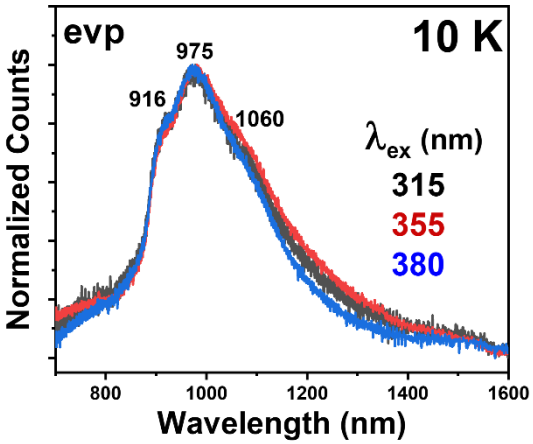

Fig. S27 The normalized (at 975 nm) NIR emission spectra at 10 K of a $Cs_2NaBiCl_6$ sample prepared by the evaporation method.

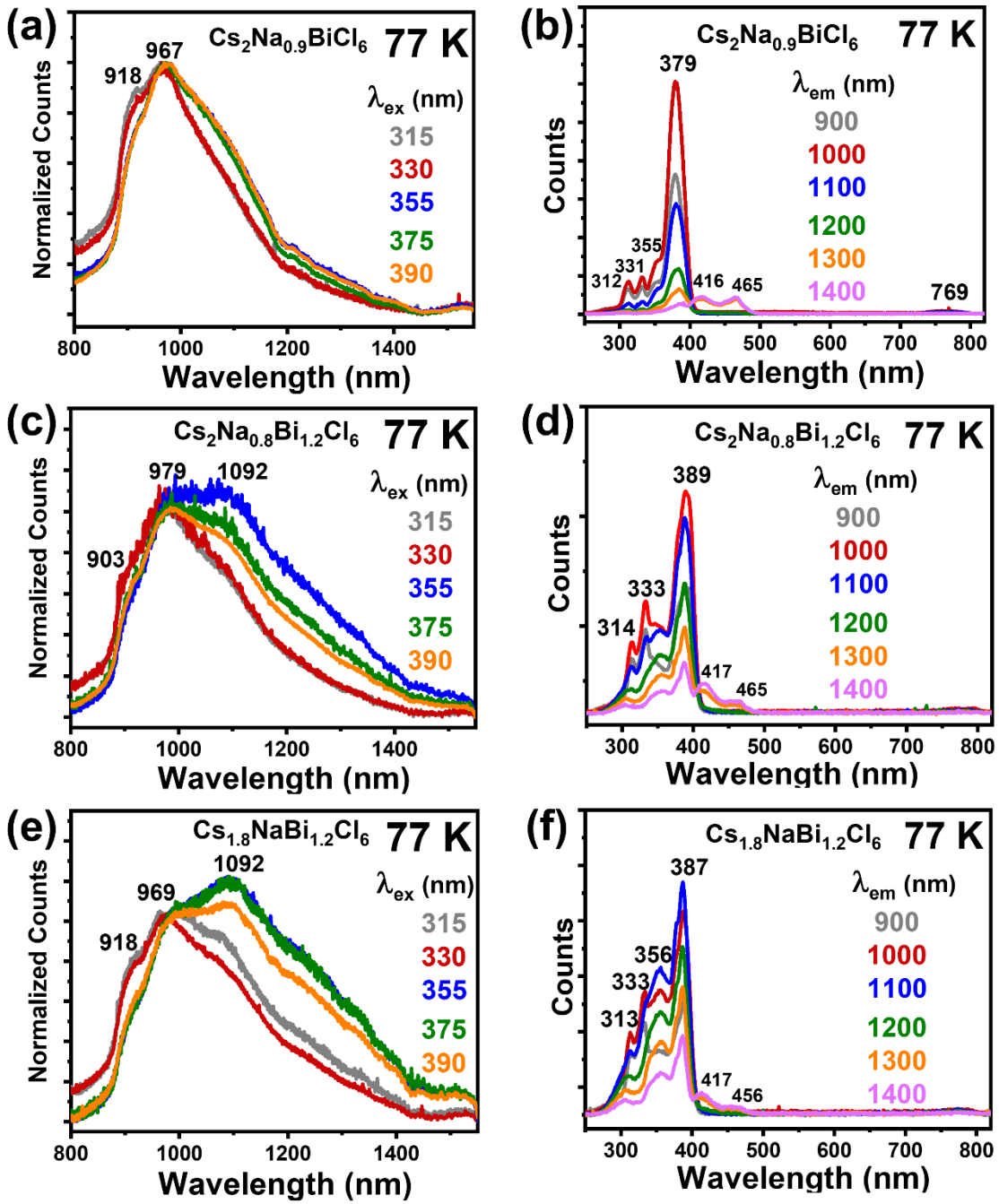

Fig. S28 77 K NIR emission and excitation spectra of nonstoichiometric samples of $Cs_2NaBiCl_6$.

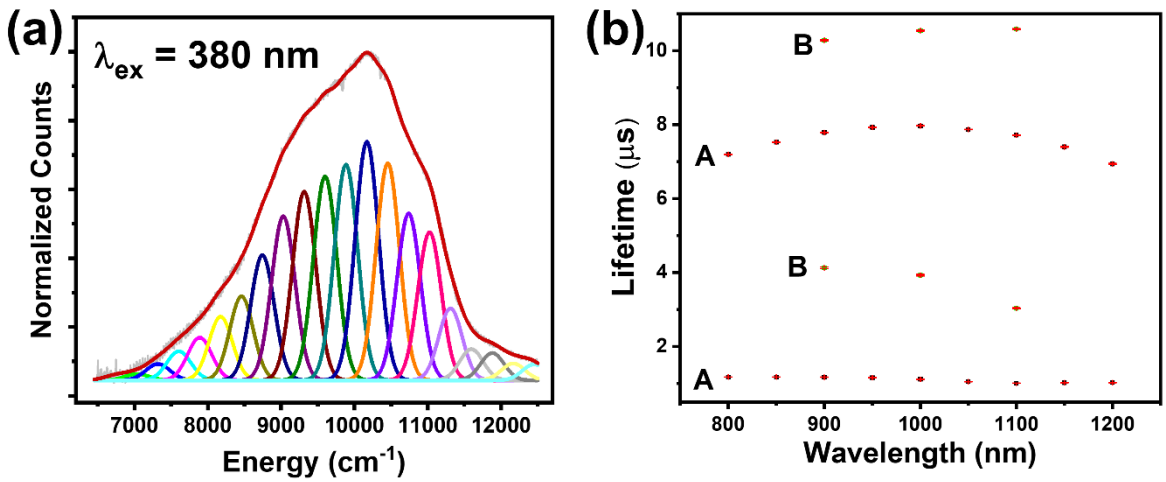

Fig. S29 (a) Deconvolution of 77 K NIR emission spectrum into Gaussian bands separated by 0.035 eV (285 cm^{-1}) between 800 nm and 1550 nm. (b) 77 K biexponential lifetime measurements across the NIR emission band. A and B are separate syntheses of $Cs_2NaBiCl_6$. The error bars in the lifetime fits are shown. The mean lifetimes across the band are, in A: τ_1 1.1±0.1 μs, τ_2 7.6±0.4 μs: B τ_1 3.7±0.6 μs, τ_2 10.5±0.2 μs.

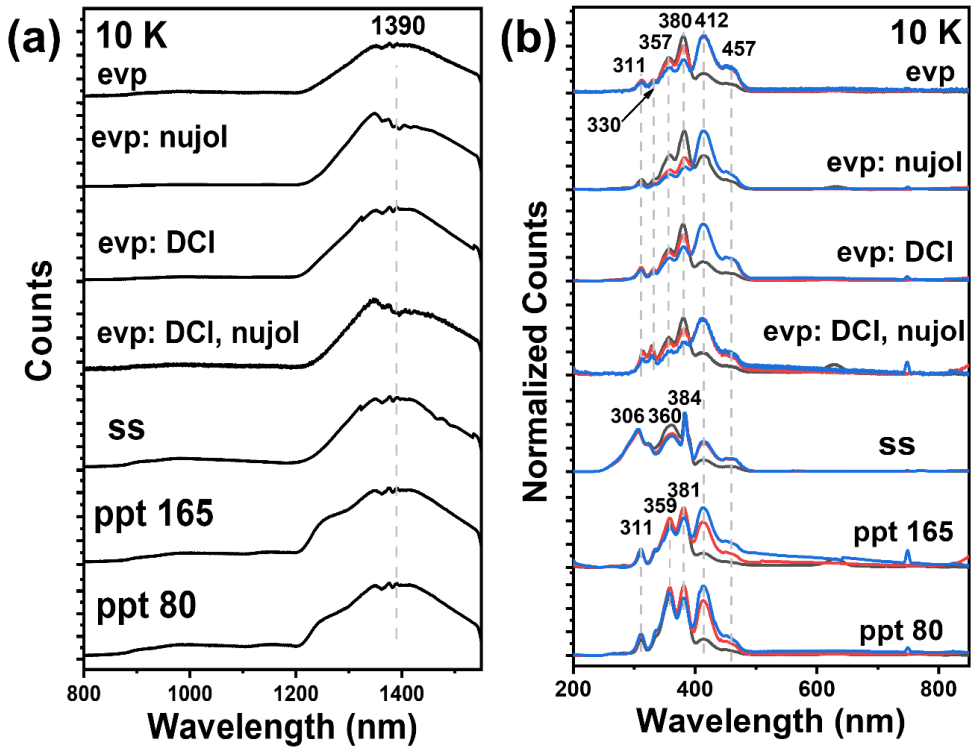

Fig. S30 IR Emission (λ_{exc} = 410 nm) and excitation spectra (λ_{em} = 1300 nm, black; 1400 nm, red; 1500 nm, blue) of $Cs_2NaBiCl_6$ samples at 10 K. The excitation spectra are generally similar except for the ss method.

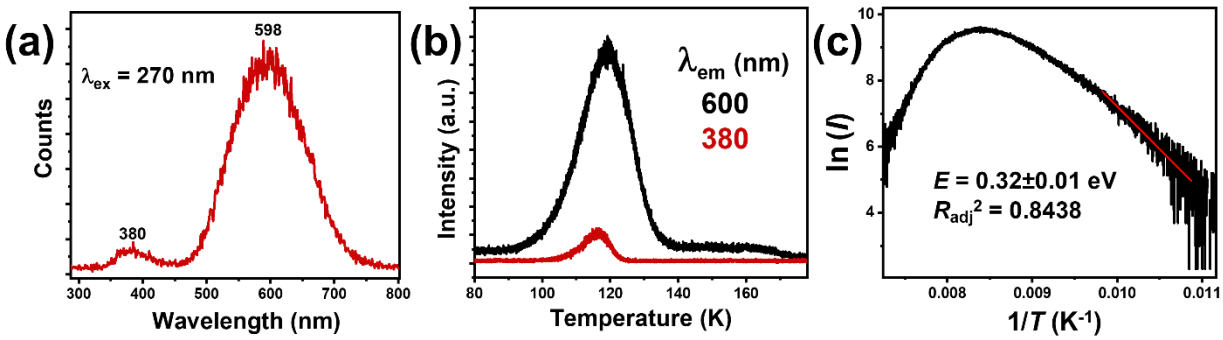

Fig. S31 (a) Persistent luminescence spectra after charging at 77 K for 10 min. (b) TL spectra (heating rate 10 K min^{-1}) monitoring 600 nm (black) and 380 nm (red) radiation. The samples were charged by 270 nm radiation for 10 min at 77 K. (c) Initial rise method applied to 600 nm TL charged by 270 nm radiation.

S8. References

1. P. E. Blöchl, Projector augmented-wave method, *Phys. Rev. B*, 1994, **50**, 17953-17979.
2. G. Kresse and J. Hafner, Ab initio molecular dynamics for liquid metals, *Phys. Rev. B*, 1993, **47**, 558-561.
3. G. Kresse and J. Hafner, Ab initio molecular-dynamics simulation of the liquid-metal– amorphous-semiconductor transition in germanium, *Phys. Rev. B*, 1994, **49**, 14251-14269.
4. J. P. Perdew, K. Burke and M. Ernzerhof, Generalized gradient approximation made simple, *Phys. Rev. Lett.*, 1996, **77**, 3865-3868.
5. M. Liu, C.-K. Duan, P. A. Tanner, C.-G. Ma and M. Yin, Rationalizing the photoluminescence of Bi^{3+} and Sb^{3+} in double perovskite halide crystals, *J. Phys. Chem. C*, 2021, **125**, 26670–26678.
6. H. Wondratschek, *The mathematical theory of symmetry in solids. Representation theory for point groups and space groups* by C. J. Bradley and A. P. Cracknell. *Acta Crystallogr. A*, 1973, **29**, 581–582.
7. H. Zheng, Z. Tang, P. Liang, H. Shu, L. Wang, J. Huang, A. A. Levin, P. N. Brunkov and Z. Liu, Intrinsic point defects in halide double perovskite $Cs_2NaBiCl_6$ insight from first-principles. *Thin Solid Films*, 2021, **732**, 138781.
8. S. Zhao, K. Yamamoto, S. Iikubo, S. Hayase and T. Ma, First-principles study of electronic and optical properties of lead-free double perovskites Cs_2NaBX_6 (B= Sb, Bi; X= Cl, Br, I), *J. Phys. Chem. Solids*, 2018, **117**, 117-121.
9. W. Shi, T. Cai, Z. Wang and O. Chen, The effects of monovalent metal cations on the crystal and electronic structures of Cs_2MBiCl_6 (M= Ag, Cu, Na, K, Rb, and Cs) perovskites, *J. Chem. Phys.*, 2020, **153**, 141101.

10. Y. Sun, A. J. Fernández-Carrión, Y. Liu, C. Yin, X. Ming, B.-M. Liu, J. Wang, H. Fu, X. Kuang, X. Xing, Bismuth-based halide double perovskite $Cs_2LiBiCl_6$: crystal structure, luminescence, and stability, *Chem. Mater.*, 2021, **33**, 5905−5916.
11. H. Shi and M.-H. Du, Discrete Electronic bands in semiconductors and insulators: potential high-light-yield scintillators, *Phys. Rev. Applied*, 2015, **3**, 054005.
12. R. Anbarasan, J. K. Sundar, M. Srinivasan and P. Ramasamy, First principle insight on the structural, mechanical, electronic and optical properties of indirect band gap photovoltaic material Cs_2NaBiX_6 (X = Cl, Br, I), *Comput. Condens. Matter.*, 2021, **28**, e00581.
13. H. Li, C. Pi, W. Chen, M. Zhou, J. Wei, J. Yi, P. Song, Y. Alexey, Y. Zhong, X. Yu, J. Qiu and X. Xu, A highly stable photodetector based on a lead-free double perovskite operating at different temperatures, *J. Phys. Chem. Lett.*, 2021, **12**, 5682–5688.
14. C. Freysoldt, B. Grabowski, T. Hickel, J. Neugebauer, G. Kresse, A. Janotti and C. G. Van de Walle, First-principles calculations for point defects in solids, *Rev. Mod. Phys.*, 2014, **86**, 253–305.
15. T. R. Durrant, S. T. Murphy, M. B. Watkins and A. L. Shluger, Relation between image charge and potential alignment corrections for charged defects in periodic boundary conditions, *J. Chem. Phys.*, 2018, **149**, 024103.
16. S. Lany and A. Zunger, Assessment of correction methods for the band-gap problem and for finite-size effects in supercell defect calculations: Case studies for ZnO and GaAs, *Phys. Rev. B*, 2008, **78**, 235104.
17. S. Lany and A. Zunger, Accurate prediction of defect properties in density functional supercell calculations, *Model. Simul. Mat. Sci. Eng.*, 2009, **17**, 084002.

18. A. Wang, R. Kingsbury, M. McDermott, M. Horton, A. Jain, S. Ping Ong, S. Dwaraknath and K. A. Persson, A framework for quantifying uncertainty in DFT energy corrections, *Sci. Reports*, 2021, **11**, 1-10.

19. A. C. Van Der Steen and G. J. Dirksen, Luminescence and crystal growth of Cs_2NaYCl_6:Bi, *Chem. Phys. Lett.*, 1978, **59**, 110-112.

20. M. Buryi, V. Babin, R. A. M. Ligthart, S. S. Nagorny, V. B. Mikhailik, V. Vaněček, L. P. Prochazková, R. Kandel, V. V. Nahornadg and P. Wang, Correlation of emission, scintillation and charge trapping properties in Cs_2HfCl_6 and Cs_2ZrCl_6 single crystals, *J. Mater. Chem. C*, 2021, **9**, 2955–2968.

21. R. Král, V. Babin, E. Mihóková, M. Buryi, V. V. Laguta, K. Nitsch and M. Nikl, Luminescence and charge trapping in Cs_2HfCl_6 single crystals: optical and magnetic resonance spectroscopy study, *J. Phys. Chem. C*, 2017, **121**, 12375–12382.

22. C. K. Jørgensen, Electron transfer spectra, *Prog. Inorg. Chem.*, 1970, **12**, 101-158.

23. V. Pagonis, G. Kitis and C. Furetta, Numerical and practical exercises in thermoluminescence, 2006, Springer Science+Business Media, Inc.

24. A. Krasnikov, E. Mihokova, M. Nikl, S. Zazubovich and Y. Zhydachevskyy, Luminescence spectroscopy and origin of luminescence centers in Bi-doped materials, *Crystals*, 2020, **10**, 208.

25. F. Pelle, B. Jacquier, J. P. Denis and B. Blanzat, Optical properties of $Cs_2NaBiCl_6$, *J. Lumin.*, 1978, **17**, 61-72.